Earth and Planetary Science Letters 552 (2020) 116594

Contents lists available at ScienceDirect

Earth and Planetary Science Letters

www.elsevier.com/locate/epsl

Trace element fractionation and isotope ratio variation during melting of a spatially distributed and lithologically heterogeneous mantle

Yan Liang

Department of Earth, Environmental and Planetary Sciences, Brown University, Providence, RI 02912, United States of America

ARTICLE INFO

Article history:
Received 13 May 2020
Received in revised form 31 August 2020
Accepted 18 September 2020
Available online 30 September 2020
Editor: R. Dasgupta

Keywords:
mantle heterogeneity
lithological heterogeneity
fractional melting
mixing
trace element
isotope ratio

ABSTRACT

The source region of basalts in the mantle is chemically and lithologically heterogeneous. During decompression melting of a spatially distributed and lithologically heterogeneous mantle, mineral modes of distinct mantle sources vary continuously, resulting in spatial and temporal variations in the bulk partition coefficient of a trace element in different lithologies in the melting column, which in turn affects the fractionation of the trace element in partial melt and residual solid. This problem can be quantified by following the motion of solid in the melting column. This study presents a new melting model that can be used to keep track of spatial and temporal variations of mineral mode, melting reaction, bulk partition coefficient, and trace element concentration in the lithologically heterogeneous melting column. Simple analytical solutions for a time-dependent perfect fractional melting model are obtained. Essential features of the new model are elucidated through case studies of melting a two-lithology mantle that consists of blobs of orthopyroxene-rich lithology in the upwelling lherzolitic mantle; and an application to Sr-Nd-Hf isotope ratio variations in basalts from the Mid-Atlantic Ridge is presented. Fractional melting of the two-lithology mantle results in large temporal variations in incompatible trace element concentrations and Sr-Nd-Hf isotope ratios in the pooled melt. Mixing of fractional melts derived from different lithologies in the melting column produces enriched and depleted melts that form mixing loops in Sr-Nd-Hf isotope ratio correlation diagrams. These mixing loops rotate away from mixing lines defined by the binary mixing model and are a unique feature of melting a spatially heterogeneous mantle. Formation of the mixing loop can be traced to the location and spacing of the enriched lithological units in the melting column. The role of lithological heterogeneity is to change the bulk partition coefficient of a trace element from its values in the lherzolitic mantle to new values in the pyroxenitic mantle, which alters the extent of depletion of the trace element in the melting column. Changing bulk partition coefficient with time and space through lithological heterogeneity can result in greater variabilities in Sr-Nd-Hf isotope ratios and highly incompatible trace element concentrations in the pooled melt. Results from this study establish a framework for systematic studies of trace element fractionation and isotope ratio variation during decompression melting of a spatially distributed and lithologically heterogeneous mantle.

1. Introduction

Variations in radiogenic isotope ratios and highly incompatible trace element abundances in oceanic basalts suggest that the melt generation regions of the mantle are heterogeneous (e.g., Zindler and Hart, 1986; White, 2010; Stracke, 2012; Hofmann, 2014). The heterogeneities are long lived and likely produced by tectonic processes involving crustal formation, crust and mantle recycling, and core-mantle interaction. There are several types of heterogeneities in the mantle. In terms of radiogenic isotope ratios, the mantle source is identified as the depleted mantle and the enriched mantle of various types (Zindler and Hart, 1986). In terms of lithology, the depleted mantle source is generally ascribed to lherzolite. The lithology of the enriched mantle is still not well constrained. It could be lherzolite, harzburgite, pyroxenite, or eclogite. In geochemical studies of mantle melting, it is convenient to distinguish two types of heterogeneity in the mantle source: chemical heterogeneity and lithological heterogeneity. Chemical heterogeneity is distinguishable from the ambient mantle only in trace element abundances and isotope ratios. Lithological heterogeneity differs from the ambient mantle both in composition and mineral mode. It has been suggested that lithological heterogeneities play an important role in producing the garnet signature in mid-ocean ridge

E-mail address: yan_liang@brown.edu.

https://doi.org/10.1016/j.epsl.2020.116594
0012-821X/

basalts (MORB) and the petrogenesis of ocean island basalts (OIB) and flood basalts (e.g., Hirschmann and Stolper, 1996; Kogiso et al., 1998; Takahashi et al., 1998; Yaxley and Green, 1998; Sobolev et al., 2000, 2007; Hirschmann et al., 2003; Prytulak and Elliott, 2007; Dasgupta et al., 2010; Lambart et al., 2016; Elkins et al., 2019). The length scale of mantle heterogeneity varies considerably, ranging from grain size in hand specimen, meters to kilometers in outcrops, kilometers to hundreds of kilometers along mid-ocean ridges. In the literature, heterogeneous mantle is often depicted as blobs of enriched mantle of various sizes and types embedded in the ambient depleted mantle. Any geochemical model for melting a heterogeneous mantle should consider the following basic features of the enriched component in the mantle source: its size, spatial distribution, lithology, and composition. The present study focuses on lithology.

Considerable progress has been made in quantifying variations of trace element abundance and isotope ratio in partial melt and residual solid during decompression melting of a spatially distributed and chemically heterogeneous mantle (DePaolo, 1996; Liang, 2008; Liu and Liang, 2017, 2020; Bo et al., 2018; Liang and Liu, 2018). In this class of melting models, the solid and melt flow fields are time-independent. The mantle source feeding into the melting column is lithologically homogeneous but compositionally time-dependent. The time-dependency arises because the enriched component has finite size. The time-dependent batch melting, fractional melting, and dynamic melting models have the same mathematical forms as the respective steady-state melting models that are widely used in the geochemical literature except the source composition in the former varies as a function of time (Liang, 2008; Liang and Liu, 2018).

There is no time-dependent model for batch melting, fractional melting, or dynamic melting of a spatially distributed and lithologically heterogeneous mantle. Previous geochemical treatment of this problem relies on time-independent melting models and mixing of melt derived from one lithology (e.g., pyroxenite) with that from another lithology (lherzolite). Compositions of the two melts are obtained from two independent calculations using the fractional melting model or the dynamic melting model for each lithology (e.g., Hirschmann and Stolper, 1996; Phipps Morgan, 1999; Ito and Mahoney, 2005; Stracke and Bourdon, 2009; Rudge et al., 2013; Wanless et al., 2014). The source composition of each lithology is homogeneous and the size and spatial distribution of lithological heterogeneity are not considered in this class of models. The size and distribution of mantle heterogeneity are important to the interpretation of isotope ratios and incompatible trace element variations in basalts and residual peridotites (Richter and Daly, 1989; DePaolo, 1996; Liang, 2008; Liu and Liang, 2017, 2020; Bo et al., 2018; Liang and Liu, 2018). The chief objective of this study is to develop a method for studying trace element fractionation during decompression melting of a spatially distributed and lithologically heterogeneous mantle.

To model decompression melting of a spatially distributed and lithologically heterogeneous mantle, one has to keep track of spatial and temporal variations of mineral mode and bulk solid-melt partition coefficient in the melting column. Once the mineral mode and the bulk partition coefficient are known, the lithology can be identified and the connection to trace element modeling becomes straightforward (Sections 2 and 3). To demonstrate the basic idea, the perfect fractional melting model of Shaw (1970) is generalized to include spatial and temporal variations in mantle source composition and lithology. Key features of the new model are explained through an illustrated example of melting a two-lithology mantle (Section 4). The role of lithological heterogeneity in producing variations in Sr-Nd-Hf concentrations and isotope ratios in the pooled melts is elucidated through comparative studies of melting a chemically heterogeneous mantle and a lithologically heterogeneous mantle (Section 5). The method developed in this study is general, and can be used to investigate variations in incompatible trace element concentrations and radiogenic isotope ratios in mantle derived samples. An application is presented in Section 5.3.

2. Mineral mode and bulk partition coefficient

2.1. Governing equations

To model trace element variations during decompression melting of a lithologically heterogeneous mantle, it is necessary to keep track of variations in mineral mode and solid-melt partition coefficients in the melting column. Consider the melting reaction involving minerals M_1, $M_2, \ldots, M_N$ that produces a unit mass of melt:

$$p_1 M_1 + p_2 M_2 + \ldots + p_N M_N = \text{melt}, \tag{1a}$$

where p_j's are coefficients of the melting reaction and their summation equals to one. The bulk solid-melt partition coefficient (k_m) and the partition coefficient according to the melting reaction (k_m^p) for a trace element are defined in the usual way (Shaw, 1970):

$$k_m = \sum_{j=1}^{N} w_j k_j, \tag{1b}$$

$$k_m^p = \sum_{j=1}^{N} p_j k_j, \tag{1c}$$

where w_j is the weight fraction of mineral j in the solid; and k_j is the mineral-melt partition coefficient for mineral j. The bulk solid-melt partition coefficient k_m depends on mineral mode, while k_m^p depends on the melting reaction. (Symbols used in this study are listed in Table 1.) The melting reaction is lithology specific. Hence both k_m and k_m^p vary as a function of lithology in the melting column. To model melting a lithologically heterogeneous mantle, one has to know how k_m and k_m^p vary spatially and temporally in the melting column. The starting point is the mineral mode in the melting column.

The volume fraction of mineral j in the melting column (ϕ_j) follows the mass conservation equation (Liang et al., 2010):

$$\frac{\partial \rho_j \phi_j}{\partial t} + \frac{\partial \rho_j \phi_j V_s}{\partial z} = -p_j \Gamma, \tag{2}$$

where t is time; z is the vertical coordinate, positive upward; ρ_j is the mineral density; V_s is the solid velocity; Γ is the melting rate of the bulk solid. The melting rate of mineral j is $p_j \Gamma$ for the melting reaction Eq. (1a). Given mineral mode, an equation governing the spatial and temporal variations of the bulk solid-melt partition coefficient in the melting column is derived (Appendix A):

$$\frac{\partial k_m}{\partial t} + V_s \frac{\partial k_m}{\partial z} = \frac{\Gamma \left(k_m - k_m^p\right)}{\rho_s \left(1 - \phi_f\right)}, \tag{3}$$

where ρ_s is the solid density and equals to the weighted sum of mineral densities; ϕ_f is the volume fraction of the melt. The left-hand-side of Eq. (3) is a material derivative following the motion of the solid. When $k_m = k_m^p$, partition coefficient of a mantle parcel does not change during its transit through the melting column, and the problem is reduced to modal melting. Eq. (3) is valid when mineral-melt partition coefficients for the trace element of interest are constant and uniform in the melting column. (A more general case of variable k_j is presented in Appendix A.)

The degree of melting experienced by a parcel of solid traveling through the melting column is given by the material derivative (Liang, 2008):

Table 1
List of key symbols.

Symbol	Description
C_f	Concentration of a trace element in the instantaneous melt (Eq. (12))
C_f^{pool}	Concentration of a trace element in the pooled melt (Eq. (15))
C_f^0, C_s^0	Concentration of the melt or bulk solid at the onset of melting
F	Degree of melting experienced by the solid matrix (Eqs. (4) & (8b))
$F_{\max}$	Maximum extent of melting at the top of the melting column (Eq. (8c))
k_m	Bulk solid-melt partition coefficient for a trace element (Eqs. (1b), (3), (5) & (9a))
k_m^p	Partition coefficient according to melting reaction (Eqs. (1c), (6b) & (9b))
p_j	Coefficient of melting reaction
t_0	Solid upwelling time scale, $t_0 = z_0/V_s^0$
t	Time
t_f	Time needed for the mantle parcel to travel from the base to its current position in the melting column (Eq. (9c))
V_f, V_s	Velocity of the melt or solid
V_s^0	Solid upwelling rate at the onset of melting
w_j	Mass fraction of mineral j in the solid
z_0	Height of the column where melting takes place
z	Vertical coordinate with origin at the bottom of the melting column
ϕ_j	Volume fraction of mineral j in the solid (Eqs. (2) & (10a))
ϕ_f	Porosity or volume fraction of the melt in the melting column
Γ	Melting rate of the bulk solid (Eq. (6a))
ρ_f, ρ_s, ρ_j	Density of the melt, bulk solid, or mineral j

$$\frac{\partial F}{\partial t} + V_s \frac{\partial F}{\partial z} = \frac{(1-F)\,\Gamma}{\rho_s\left(1-\phi_f\right)}, \tag{4}$$

where the factor 1-F accounts for the fact that F fraction of fusible solid has already been converted to melt in the melting column. A useful equation can be obtained by combining Eqs. (3) and (4):

$$\frac{\partial\,(1-F)\,k_m}{\partial t} + V_s \frac{\partial\,(1-F)\,k_m}{\partial z} = -\frac{(1-F)\,\Gamma k_m^p}{\rho_s\left(1-\phi_f\right)}. \tag{5}$$

The product, $(1-F)\,k_m$, appears in non-modal melting models (see Eq. (9a) below). Since different lithologies may have different melting rate and melting reaction, material derivatives are used to keep track of Γ and k_m^p in the melting column:

$$\frac{\partial \Gamma}{\partial t} + V_s \frac{\partial \Gamma}{\partial z} = 0, \tag{6a}$$

$$\frac{\partial k_m^p}{\partial t} + V_s \frac{\partial k_m^p}{\partial z} = 0. \tag{6b}$$

Eqs. (6a) and (6b) are valid when the melting rate and melting reaction for a mantle parcel are constant during its transit through the melting column. Different lithologies may have different melting rates and melting reactions. For variable melting rate and melting reaction, a source term based on thermodynamics of melting and melting reaction should be added to the right-hand-side of Eqs. (6a) and (6b).

Given the solid velocity, melting rate and melting reaction of each lithology, and boundary conditions at the bottom of the melting column ($z = 0$), Eqs. (2)-(6) can be used to calculate mineral mode, bulk partition coefficient, and extent of melting experienced by the solid in the melting column. An example is provided below.

2.2. Melting a modally heterogeneous mantle

Let us consider a simplified problem in which the enriched lithology has the same melting rate and solidus as the ambient mantle, but different starting composition, mineral mode, and melting reaction. This reduced problem, which is called *melting a modally heterogeneous mantle* hereafter, admits simple analytical solutions and is sufficient to demonstrate key features of the time-dependent model. For purpose of demonstration, it is assumed that the melting rate is constant and uniform (i.e., $\Gamma = \Gamma_0$), the solid velocity (V_s) is independent of time, and the porosity in the melting column is very small (i.e., $\phi_f \ll 1$). These simplifications have been widely used in geochemical modeling of mantle melting. The time-dependent boundary conditions for this problem are:

$$\phi_j\,(t,0) = \phi_j^0\,(t)\,, \tag{7a}$$

$$k_m\,(t,0) = k_m^0\,(t)\,, \tag{7b}$$

$$k_m^p\,(t,0) = k_m^{p0}\,(t)\,, \tag{7c}$$

$$F\,(t,0) = 0, \tag{7d}$$

where ϕ_j^0, k_m^0, and k_m^{p0} are the volume fraction of mineral j, bulk partition coefficient, and partition coefficient for the melting reaction at the bottom of the melting column ($z = 0$), respectively.

For melting in an upwelling mantle column, it is convenient to nondimensionalize the time (t) and vertical coordinate (z) in Eqs. (2)-(6) by the solid upwelling time ($t_0 = z_0/V_s^0$) and the height of the melting column (z_0), where V_s^0 is the upwelling velocity at $z = 0$. For $z_0 = 60$ km and $V_s^0 = 60$ mm/yr, the upwelling time is 1 Myr. Under the condition stated in the preceding paragraph, the dimensionless solid velocity decreases and the degree of melting increases upward in the melting column:

$$V_s\,(z) = 1 - F_{\max} z, \tag{8a}$$

$$F\,(z) = F_{\max} z, \tag{8b}$$

$$F_{\max} = \frac{\Gamma_0 z_0}{\rho_s V_s^0}, \tag{8c}$$

where F_{max} is the degree of melting at the top of the melting column ($z = 1$); z is the dimensionless vertical coordinate, varying between 0 and 1.

Given V_s, F, and boundary conditions Eqs. (7b) and (7c), the partition coefficients can be solved from Eqs. (5) and (6b) using the method of characteristics. Integrating Eqs. (5) and (6b) along a characteristic line, we have the following expressions for the time-dependent problem:

$$k_m(t,z) = \frac{k_m^0(t-t_f) - k_m^{p0}(t-t_f)F(z)}{1-F(z)}, \tag{9a}$$

$$k_m^p(t,z) = k_m^{p0}(t-t_f), \tag{9b}$$

$$t_f = -\frac{1}{F_{\max}}\ln(1-F_{\max}z), \qquad 0 \le z \le 1, \tag{9c}$$

where t is the dimensionless time; t_f is the time needed for the mantle parcel to travel from the base ($z=0$) to its current position (z) in the melting column. For $F_{max}=0.2$ and $z=1$, $t_f=1.12$, i.e., it takes 1.12 Myr for the mantle parcel to transit through the melting column if the upwelling time is 1 Myr. The longer transit time is due to the reduction of solid velocity in the melting column (Eq. (8a)). The function notation $k_m^0(t-t_f)$ means: given the functional form $k_m^0(t)$ of variable t, $k_m^0(t-t_f)$ is obtained by replacing the original variable t by the new variable $t-t_f$.

Eqs. (9a)-(9c) are valid for $t \ge t_f$, i.e., when all the materials in the melting column at $t=0$ are advected out of the melting column (Liang, 2008). (Solutions for $t < t_f$ depend on initial condition of the melting column, which is not relevant to melting beneath mid-ocean ridges.) Eq. (9a) recovers the familiar expression for the bulk partition coefficient (Shaw, 1970) when the mantle source at the base of the melting column is modally homogeneous. To compute the bulk partition coefficient in a modally heterogeneous melting column, one follows the motion of residual solid. This expected result is quantified by the travel time through Eq. (9c).

In deriving Eq. (9a), no additional information on mineral mode and melting reaction was used. For the simple problem considered here, Eqs. (2) and (7a) can be solved exactly. The volume fraction and weight fraction of mineral j are given by the expressions:

$$\phi_j(t,z) = \frac{\phi_j^0(t-t_f) - \frac{\rho_s}{\rho_j}p_j(t-t_f)F(z)}{1-F(z)}, \tag{10a}$$

$$w_j(t,z) = \frac{w_j^0(t-t_f) - p_j(t-t_f)F(z)}{1-F(z)}, \tag{10b}$$

where t_f is the same as Eq. (9c). When a mineral is consumed by melting reaction (i.e., $p_j > 0$), its modal abundance decreases upward in the melting column. The degree of melting at which mineral j in the mantle parcel is completely consumed by the melting reaction (F_j^{out}) is given by:

$$F_j^{out} = \frac{w_j^0(t-t_f)}{p_j(t-t_f)}. \tag{11}$$

Multiply Eq. (10b) by the mineral-melt partition coefficient k_j and sum over all the minerals, Eq. (9a) is recovered. The preceding example demonstrates the consistency of the evolution equations (Eqs. (3) and (5)) in tracking variations of the bulk partition coefficient in the melting column. An example of calculated mineral modes and trace element partition coefficients using Eqs. (9a)-(9c), and (10b) are presented in Section 4.

3. Trace element fractionation

3.1. Mass conservation equation for a trace element

Neglecting diffusion and dispersion in the melt, mass conservation equation for a trace element in the heterogeneous melting column can be written as (Liang and Peng, 2010):

$$\left[\rho_f\phi_f + \rho_s(1-\phi_f)k_m\right]\frac{\partial C_f}{\partial t} + \left[\rho_f\phi_f V_f + \rho_s(1-\phi_f)V_s k_m\right]\frac{\partial C_f}{\partial z} = (k_m^p - 1)C_f\Gamma. \tag{12}$$

Eq. (12) is valid when the interstitial melt and residual solid are in local chemical equilibrium and the mineral-melt partition coefficient is constant and uniform in the melting column. (A more general equation that includes variable mineral-melt partition coefficient is presented in Appendix B.) Eq. (12) recovers the mass conservation equation of McKenzie (1984) when $k_m^p = k_m$ (i.e., modal melting). It is important to note that mineral mode and lithology do not appear explicitly in Eq. (12). Instead, they are encapsulated in the partition coefficients (k_m and k_m^p) through the assumption of local chemical equilibrium between the melt and residual solid. Hence to model trace element fractionation during melting of a lithologically heterogeneous mantle, it is sufficient to keep track of variations in the solid-melt partition coefficients in the melting column. This underscores the importance of the evolution equations for the partition coefficients (Eqs. (3) and (6b)), a point that is further demonstrated below.

3.2. Perfect fractional melting of a modally heterogeneous mantle

Perfect fractional melting is arguably the most widely used melting model for trace element fractionation in the geochemical literature. During perfect fractional melting, any melt generated in the melting column is instantaneously removed from residual solid. Setting $\phi_f = 0$ in Eq. (12), we have

$$\frac{\partial C_f}{\partial t} + V_s\frac{\partial C_f}{\partial z} = \frac{(k_m^p - 1)C_f\Gamma}{\rho_s k_m}. \tag{13a}$$

Consider the general time-dependent boundary condition at $z=0$:

$$C_f^0(t,0) = \frac{C_s^0(t)}{k_m^0(t)}, \tag{13b}$$

where C_s^0 is the lithology-dependent mantle source composition. As before, we scale t and z in Eqs. (13a) and (13b) by the upwelling time (t_0) and the column height (z_0) and solve the dimensionless equation using the method of characteristics. The solution for the instantaneous melt is:

$$C_f(t,z) = \frac{C_s^0(t-t_f)}{k_m^0(t-t_f)}\left[1 - \frac{k_m^{p0}(t-t_f)}{k_m^0(t-t_f)}F\right]^{\frac{1-k_m^{p0}(t-t_f)}{k_m^{p0}(t-t_f)}}, \tag{14}$$

where the function notation, travel time (t_f), and partition coefficients (k_m and k_m^p) are the same as those in Eqs. (9a)-(9c).

The composition of the aggregated or pooled melt (C_f^{pool}) at the top of the melting column ($z=1$) depends on the mechanism and the rate of melt extraction through a channel network. In the case of instantaneous melt extraction, the pooled melt at a given time (t) equals to the composition of average melt in the melting column at time t:

$$C_f^{pool}(t) = \frac{1}{F_{\max}}\int_0^{F_{\max}} C_f(t,F)\,dF = \int_0^1 C_f(t,z)\,dz. \tag{15}$$

If the rate of melt extraction through the channel network is finite, one has to consider the transport process in high-porosity channels (see Eq. B7a in Liang and Liu, 2018).

Eq. (14) recovers the time-dependent perfect fractional melting model for melting of a chemically heterogeneous mantle when the partition coefficients in the starting mantle are constant (Liang and Liu, 2018). Eqs. (14) and (15) reduce to the familiar expressions for perfect fractional melting (Shaw, 1970) when both partition coefficients and composition of the mantle source are independent of time. Eq. (15) is a more general mixing model: it is a

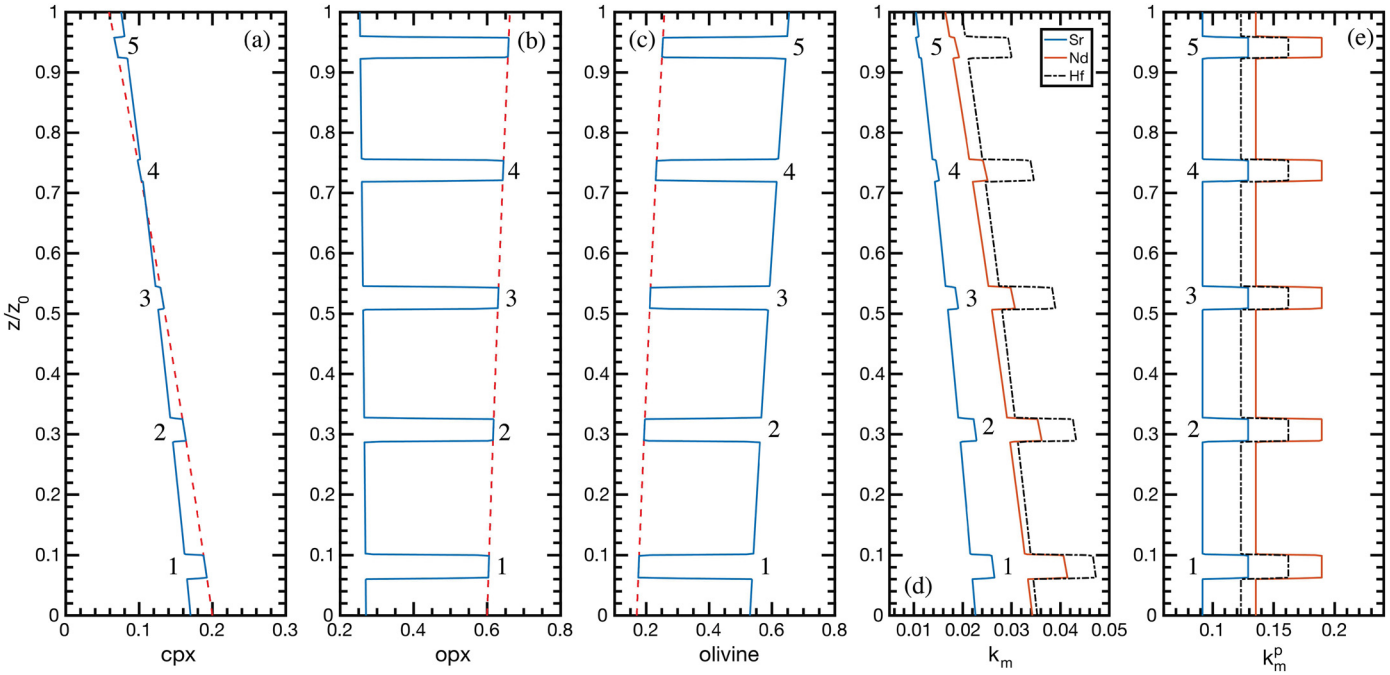

Fig. 1. Spatial variations of modal abundances of clinopyroxene (cpx, panel a), orthopyroxene (opx, b), and olivine (c), Sr, Nd, and Hf bulk partition coefficients (d), and Sr, Nd, and Hf partition coefficients for melting reaction (e) in the melting column at a selected time. A train of enriched layers enters the melting column at 0.233 units a time from below ($z = 0$). Numbers 1 to 5 mark the enriched layers at the given time in the melting column. For comparison, modal abundances for melting the pure enriched mantle are shown as red dashed lines in (a)-(c). The maximum extent of melting is 15% at the top of the melting column. (For interpretation of the colors in the figure(s), the reader is referred to the web version of this article.)

recipe for mixing melts derived from the enriched and depleted mantle sources in accordance with their size and spatial distribution in the melting column. This is a key difference between the time-dependent and the time-independent melting models. Eqs. (9), (14), and (15) constitute a complete recipe for modeling trace element fractionation during perfect fractional melting of a modally heterogeneous mantle. To calculate trace element concentration in the instantaneous melt during perfect fractional melting, one follows the motion of residual solid in the melting column. The trajectory or locus of a mantle parcel in the melting column is given by Eq. (9c).

4. An illustrated example

To highlight essential features of the time-depending fractional melting model, let us consider variations in melting parameters and melt compositions during decompression melting of a two-component mantle that consists of the ambient depleted mantle (designated as DM) and blobs (layers in 1D) of enriched mantle (EM). The lithology of DM is spinel lherzolite (17% cpx + 27% opx + 53% olivine + 3% spinel). The lithology of EM is an opx-rich websterite (20% cpx + 60% opx + 17% olivine + 3% spinel) which is used here to demonstrate the capability of the new model. Pyroxene-rich lithology can be formed by melt-rock reaction in the deep mantle prior to the onset of spinel lherzolite melting. Melting reaction for the lherzolite is based on pMELTS (Walter, 2014):

$$0.70\ \text{cpx} + 0.36\ \text{opx} + 0.10\ \text{spinel} = 0.18\ \text{olivine} + \text{melt}. \quad (16a)$$

Based on melting reactions for cpx-rich websterite (Lambart et al., 2009; Borghini et al., 2017), the following melting reaction for the enriched mantle is used in the example below:

$$1.0\ \text{cpx} + 0.25\ \text{opx} + 0.075\ \text{spinel} = 0.33\ \text{olivine} + \text{melt}. \quad (16b)$$

The higher melting rate of cpx in Eq. (16b) is used here to simulate higher melting rate of the enriched component while keeping the bulk melting rate of the enriched mantle the same as the depleted mantle.

Figs. 1a-1e present a snap shot of spatial variations of modal abundances of clinopyroxene (cpx), orthopyroxene (opx), and olivine and partition coefficients of Sr, Nd, and Hf in the melting column. Here we consider a train of EM that are initially identical in size (thickness = 0.04 or 2.4 km for a 60 km melting column) and evenly spaced in the ambient DM. The center-to-center distance between adjacent layers is 0.233 dimensionless units (14 km) and the volume fraction of EM in the mantle source is 17.2%. (The high EM volume fraction used here is to aid visualization.) Since the initial sizes of the enriched layers are the same, Figs. 1a-1e can also be used to illustrate temporal evolution of a specific layer (say 1) as it transits upward through the melting column (from 1 to 2, to ... 5). As shown in Figs. 1a-1c, abundances of cpx, opx, and olivine in the enriched layers 1 to 5 follow the red dashed lines defined by melting reaction Eq. (16b), while the depleted mantle follows lines defined by melting reaction Eq. (16a). The starting EM has more pyroxene than the starting DM. Hence the bulk partition coefficients for Sr, Nd, and Hf are larger in the enriched layers than in the lherzolitic mantle in the lower part of the melting column (Fig. 1d). Since the melting rate of cpx in the enriched layers is higher in this example, the abundance of cpx in the enriched layer is lower in the upper part of the melting column (Fig. 1a). Consequently, the bulk partition coefficients of Sr, Nd, and Hf are lower in the enriched layer in the upper part of the melting column (Fig. 1d). When the stoichiometric coefficients for the melting reaction and mineral-melt partition coefficients are constant and uniform in the melting column, partition coefficients for the melting reaction take on constant values within the enriched and depleted layers (Fig. 1e). Fig. 1e shows that the thickness of the initially 0.04 units enriched layer decreases upward in the melting column. This is due to upward reduction in solid velocity as a result of melting and melt extraction (Eq. (8a)). A movie detailing the spatial and temporal variations is provided in the supplementary materials (Movie_1.mp4).

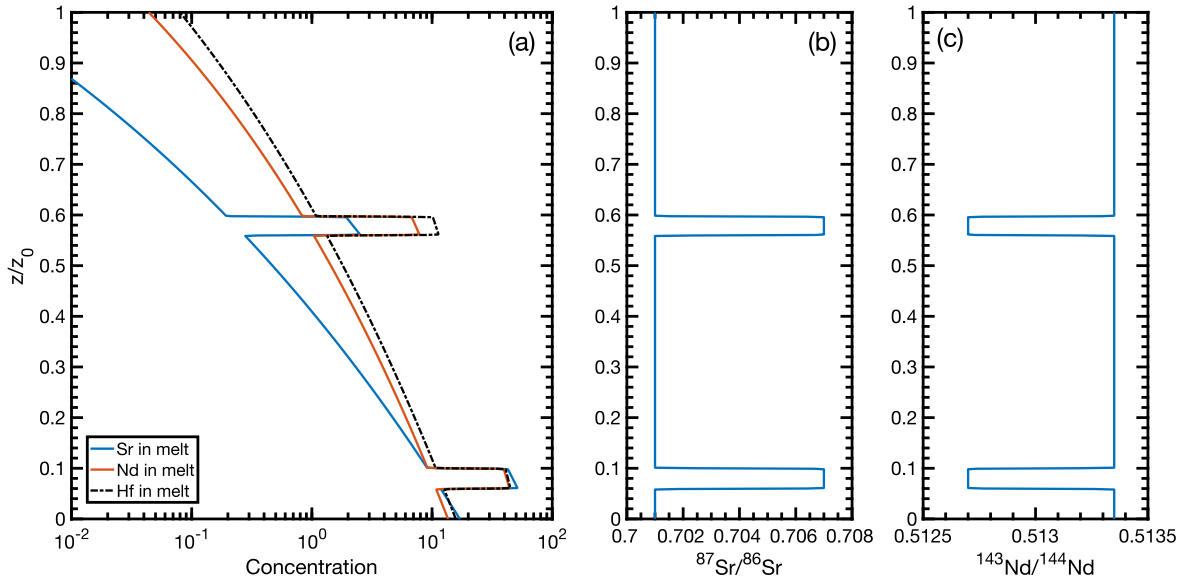

Fig. 2. Spatial variations of Sr, Nd, and Hf concentrations (panel a) and $^{87}Sr/^{86}Sr$ and $^{143}Nd/^{144}Nd$ (panels b and c) in instantaneous melt in the melting column at a given time. Concentrations of Sr, Nd, and Hf in the enriched mantle source are 5 times of those in the depleted mantle source (DMM of Workman and Hart, 2005) at the onset of melting. The volume fraction of EM in the mantle source is 7.62%. The maximum extent of melting is 15% at the top of the melting column. Concentrations are normalized by the primitive mantle of McDonough and Sun (1995).

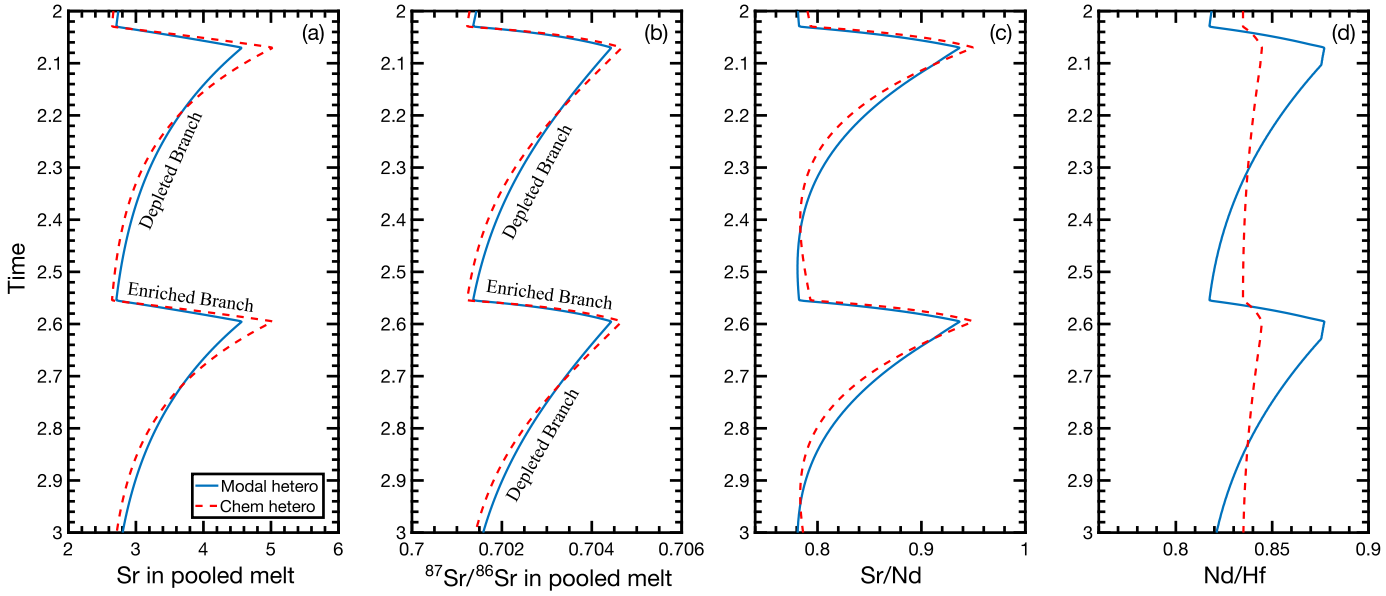

Fig. 3. Temporal variations of Sr, $^{87}Sr/^{86}Sr$, Sr/Nd, and Nd/Hf in the pooled melt produced by melting a modally heterogeneous mantle (solid lines) and a chemically heterogeneous mantle (dashed red lines). A train of enriched layers enters the melting column at 0.525 units a time from below ($z = 0$). The volume fraction of EM in the mantle source is 7.62%. The maximum extent of melting is 15% at the top of the melting column. Concentrations are normalized by the primitive mantle of McDonough and Sun (1995).

Fig. 2 presents a snap shot of spatial variations of Sr, Nd, and Hf concentrations and $^{87}Sr/^{86}Sr$ and $^{143}Nd/^{144}Nd$ in the instantaneous melts in the melting column calculated using Eq. (14) and melting parameters similar to those shown in Fig. 1, except the spacing between two adjacent enriched mantle parcels is 0.525 units apart (31.5 km for a 60 km melting column). The volume fraction of EM in the mantle source is 7.62%, a value that is more relevant to MORB petrogenesis. There are 2 to 21/2 EM parcels in the melting column at a given time in the melting column (see supplementary Movie_2.mp4). Concentration profiles of Sr, Nd, and Hf in the instantaneous melt can be described by superpositions of melts produced by fractional melting of DM and EM in accordance to their locations in the melting column. The enriched chemical signals as marked by Sr, Nd, and Hf concentrations or their isotope ratios follow the lithological heterogeneities in the melting column. The chemical and lithological heterogeneities are coupled. This is a unique feature of perfect fractional melting as there is no melt percolation in the melting column.

Compositions of the pooled melt depend on locations of the enriched mantle parcels in the melting column, and hence vary as a function of time. Figs. 3a and 3b display temporal variations of Sr and $^{87}Sr/^{86}Sr$ in the pooled melt calculated using Eq. (15) for the case illustrated in Fig. 2. As a train of identical and evenly spaced enriched mantle parcels passes through the melting column from below, Sr abundance and $^{87}Sr/^{86}Sr$ in the pooled melt zigzag between minimum values and maximum values. The maxi-

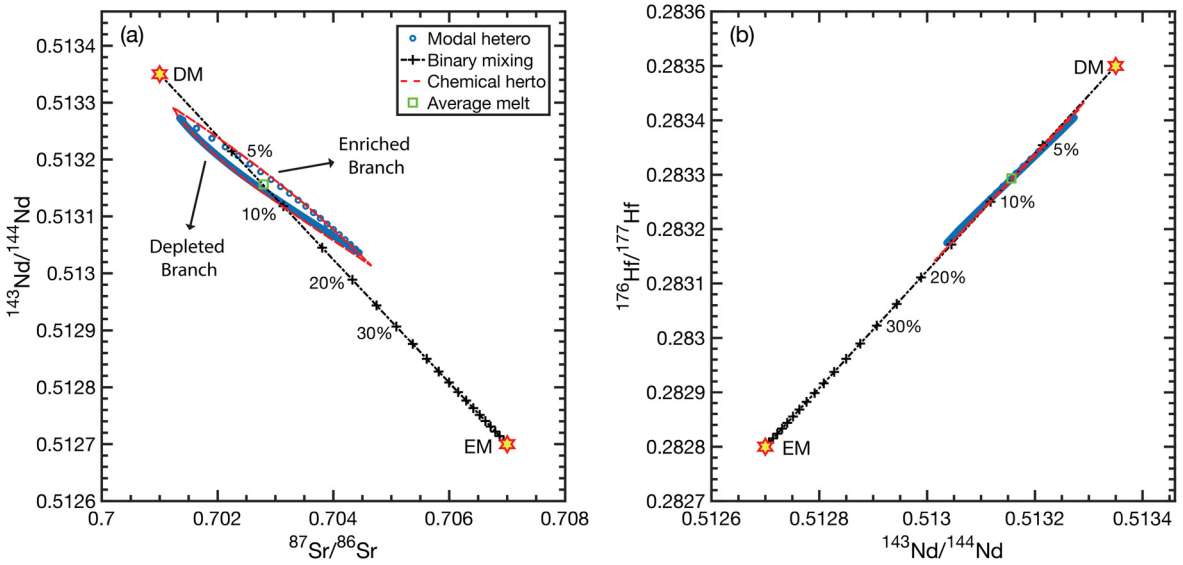

Fig. 4. Covariations of Sr-Nd-Hf isotope ratios in the pooled melt produced by melting a modally heterogeneous mantle (blue circles) and a chemically heterogeneous mantle (dashed red lines). For reference, binary mixing lines derived from mixing of pooled melts produced by 15% fractional melting of the pure DM and EM are shown as dash-dotted lines. Numbers in percentage are fractions of EM-derived melt in the binary mixture. Melting parameters are the same as those described in the caption to Fig. 2.

mum corresponds to the time when an enriched mantle parcel has just completed its transit through the bottom of the melting column (e.g., $t = 2.07$ or 2.596). The small-degree melt produced by the newly arrived enriched mantle parcel has the highest Sr abundance and hence contributes the most to the overall Sr budget in the pooled melt. The minimum corresponds to a time just before the entrance of an enriched mantle parcel into the melting column from below (e.g., $t = 2.025$ or 2.554). The enriched mantle parcels in the melting column have already been variously depleted in Sr by fractional melting (Fig. 2a), and hence contribute less to the overall Sr budget in the pooled melt. In general, abundance and isotope ratio of an incompatible trace element in the pooled melt are dominated by the composition of residual mantle in the lowest part of the melting column where the degree of melting is small and concentration of the incompatible trace element in the instantaneous melt is high.

In the $^{143}Nd/^{144}Nd$ vs. $^{87}Sr/^{86}Sr$ correlation diagram (Fig. 4a), the pooled melts define an elongated loop that is rotated counter-clockwise from the simple mixing line defined by the two end-member mantle sources (DM and EM). The counter-clockwise rotation arises because Sr is more incompatible, hence has shorter residence time in the melting column, than Nd during mantle melting (Liu and Liang, 2020). Since Hf is slightly less incompatible than Nd (Fig. 1d), one observes a small clockwise rotation in the $^{176}Hf/^{177}Hf$ vs. $^{143}Nd/^{144}Nd$ correlation diagram (Fig. 4b). The elongated loop, which is referred to as the *mixing loop* hereafter, results from mixing of melts derived from the depleted mantle and the enriched mantle parcels in the melting column. The mixing loop has an enriched branch and a depleted branch (Fig. 4a). The enriched branch corresponds to the rapid rise of Sr, $^{87}Sr/^{86}Sr$ (and fall of $^{143}Nd/^{144}Nd$) and Sr/Nd ratio in the pooled melt (Figs. 3a-3c) when an enriched mantle parcel passes through the bottom of the melting column (e.g., for $t = 2.025$ to 2.07). The deleted branch corresponds to the gradual decrease of Sr, $^{87}Sr/^{86}Sr$ (and increase of $^{143}Nd/^{144}Nd$) and Sr/Nd ratio in the pooled melt as the enriched signal in the pooled melt is being diluted by continuous melting of the depleted mantle. Hence the enriched loop is produced by mixing of the EM-derived melt in the lowest part of the melting column with the variously depleted melts in the overlying melting column. The depleted loop is formed by mixing of the DM-derived melt in the lowest part of the melting column with melts in the upper part of the melting column where the signal strength of the enriched mantle is being diluted by higher extent of melting. In the example shown in Fig. 4, samples in one enriched branch account for 7.62% of the total samples in a complete mixing loop, which is the same as the volume fraction of EM in the mantle source. This is a general result for melting a lithologically heterogeneous mantle: the proportion of samples from the enriched and depleted branches in a mixing loop is proportional to the volume fractions of EM and DM in the mantle source. A time-lapse movie detailing the rises and falls of Sr and Nd concentrations, Sr/Nd ratio, and isotope ratios in the melting column and the pooled melt is provided in the supplementary materials (Movie_2.mp4).

5. Discussion

The preceding examples demonstrate the basic features of melting an upwelling and modally heterogeneous mantle. The chemical features, in particular, are general and independent of the choice of melting reactions for the pyroxenite. For example, use of melting reactions for the cpx-rich websterite reported in the literature (Lambart et al., 2009; Borghini et al., 2017) will change calculated cpx mode and bulk partition coefficients in the pyroxenite in the upper part of the melting column but does not lead to any significant changes to the calculated melt compositions, as Sr, Nd, and Hf are fractionated mostly in the lower part of the melting column. In supplementary Figs. S1-S4, we recalculate the examples shown in Figs. 1–4 using the melting reaction of Borghini et al. (2017) for cpx-rich websterite at 1 GPa. Except for mineral modes and bulk partition coefficients (cf. Fig. 1 and Fig. S1), the results are almost indistinguishable from those shown in Figs. 1–4. In this section, we further explore the new model by addressing the following questions: (1) How do modal heterogeneities affect Sr, Nd, and Hf isotope ratios in the pooled melt? (2) What are the differences and similarities between the time-dependent mixing model (Eq. (15)) and the binary mixing model used in the literature? Answers to these questions are useful to the interpretation of Sr, Nd, and Hf isotope ratios observed in basalts.

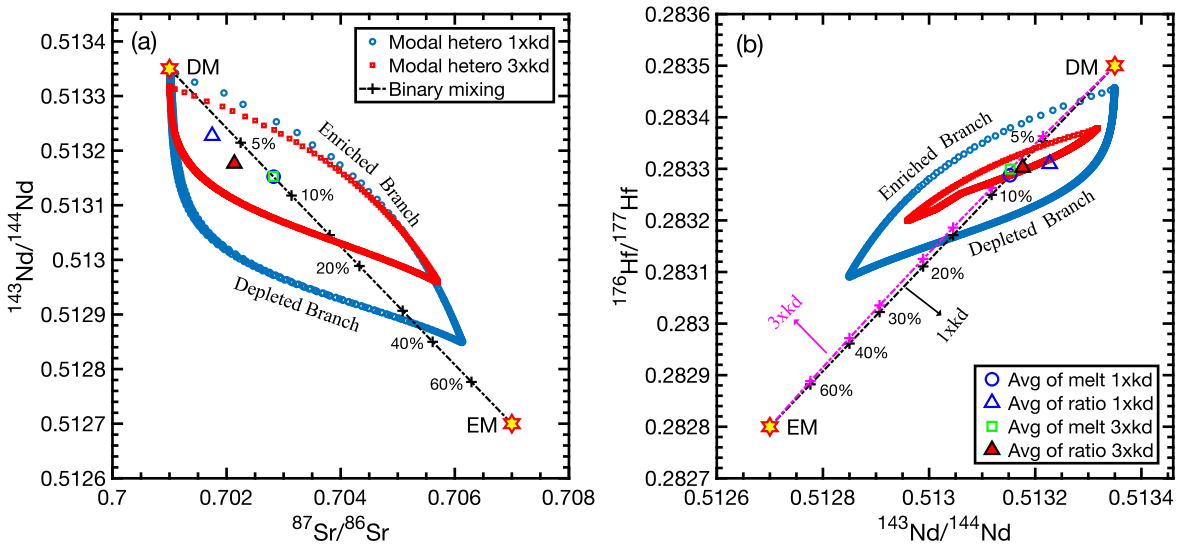

Fig. 5. Similar to Fig. 4 except the enriched lithology is a clinopyroxene-free olivine orthopyroxenite (17% olivine + 80% opx + 3% spinel, blue circles). Two cases are presented: Sr, Nd, and Hf opx-melt partition coefficients in one case (red squares) are three time of those in the other case (blue circles). For purpose of demonstration, the melting reaction of harzburgite from Baker and Stolper (1994) is used to calculate the bulk partition coefficients for the enriched lithology. Other melting parameters are the same as those described in the caption to Fig. 2.

5.1. Modal vs. chemical heterogeneity: importance of bulk partition coefficient

Figs. 3 and 4 compare Sr, Sr/Nd, Nd/Hf, $^{87}Sr/^{86}Sr$, $^{143}Nd/^{144}Nd$, and $^{176}Hf/^{177}Hf$ in pooled melts produced by melting a modally heterogeneous mantle (solid lines or blue circles) with those produced by melting a chemically heterogeneous mantle (red dashed lines) under otherwise identical conditions. The mineral mode in the enriched mantle is the same as that in the depleted mantle in the chemical heterogeneity model. In the absence of modal heterogeneity, bulk partition coefficients of Sr, Nd, and Hf in the enriched mantle parcel follow values for the lherzolitic mantle which are lower than the pyroxene-enriched layer (Fig. 1d). Consequently, Sr, $^{87}Sr/^{86}Sr$, $^{143}Nd/^{144}Nd$, and $^{176}Hf/^{177}Hf$ in the pooled melt have larger ranges of variations than in the case of the modally heterogeneous mantle (cf. the dashed and solid lines in Figs. 3, 4). However, the differences between the two cases are small, as the differences in bulk partition coefficients between the two cases are small (Fig. 1d).

Depending on lithology, bulk partition coefficients of Sr, Nd, and Hf in the enriched mantle can be smaller than those in the depleted mantle. Fig. 5 explores an extreme case in which the lithology of the enriched mantle source is a cpx-free olivine orthopyroxenite (blue circles). Clinopyroxene-free orthopyroxenite can be formed by reacting eclogite-derived melt with lherzolite between 1 and 2 GPa (Morgan and Liang, 2005; Lo Cascio, 2008; Wang et al., 2020). In the absence of cpx, bulk partition coefficients of Sr and Nd in the enriched lithology at the onset of melting (0.0021 and 0.0075) are considerably smaller than those in the depleted mantle (0.023 and 0.034), whereas partition coefficient of Hf in the enriched lithology (0.03) is slightly smaller than in the depleted mantle (0.035). Hence Sr and Nd are highly incompatible and Hf is moderately incompatible in the enriched orthopyroxenite mantle source. Consequently, the net contributions of Sr, Nd, and Hf from the enriched mantle to the pooled melt are enhanced for the enriched branch at the bottom of the melting column and concentrations of Sr, Nd, and Hf in the instantaneous melt are higher than in the case of larger partition coefficients. This explains the expanded ranges and larger variations of the mixing loops compared to the case shown in Fig. 4. The nearly vertical trend in the mixing loop closer to the DM endmember in Fig. 5a is due to the larger difference in the bulk partition coefficient between Sr and Nd in the enriched lithology ($k_{Sr}/k_{Nd} = 0.0021/0.0075$ vs. 0.023/0.034): Sr in the enriched mantle parcel is exhausted earlier and faster than Nd in the enriched mantle parcel than in the ambient mantle. This can be visualized in the supplementary animation Movie_3.mp4. (A similar explanation applies to the nearly vertical trend in Fig. 5b.)

Depending on Al, Ca, and Mg contents in opx, Sr, Nd and Hf partition coefficients in opx produced by melt-rock reaction can vary by factors of 5 to 8 (Yao et al., 2012; Sun and Liang, 2013; unpublished data). The effect of a higher opx-melt partition coefficient is to reduce the range of Sr-Nd-Hf isotopic variations in the pooled melt. This is illustrated in Fig. 5 in which the opx-melt partition coefficients for Sr, Nd, and Hf are increased by a factor of 3 for the enriched mantle (small red squares, labeled as 3xkd) compared to the extreme case discussed above (blues circles, labeled as 1xkd). The preceding examples (Figs. 4 and 5) demonstrate the importance of bulk partition coefficient and its relative difference between the enriched and depleted mantle sources to the interpretation of Sr, Nd, and Hf isotope ratios in the pooled melt. The bulk partition coefficients are determined by the lithology and melting reaction of the enriched and depleted mantle sources. Large rotation or deviation from simple mixing line in $^{176}Hf/^{177}Hf$ vs. $^{143}Nd/^{144}Nd$ correlation diagram such as the one shown in Fig. 5b maybe indicative of lithological heterogeneity in the mantle source, because Nd and Hf are more fractionated from each other in orthopyroxenite ($k_{Nd}/k_{Hf} = 0.0075/0.03$) than in lherzolite ($k_{Nd}/k_{Hf} = 0.034/0.035$).

5.2. Comparison with binary mixing model

Two component mixing has been widely used in the interpretation of variations in radiogenic isotope ratios and highly incompatible trace elements and elemental ratios in basalts (Vollmer, 1976; Langmuir et al., 1978). Figs. 4–6 present binary mixing curves calculated by adding various proportions of the pooled fractional melt derived from the pure enriched mantle to the pooled fractional melt derived from the lherzolitic mantle. Because Sr, Nd, and Hf concentrations in the two endmember melts are independent of time, binary mixing produces a single point on the mixing curve

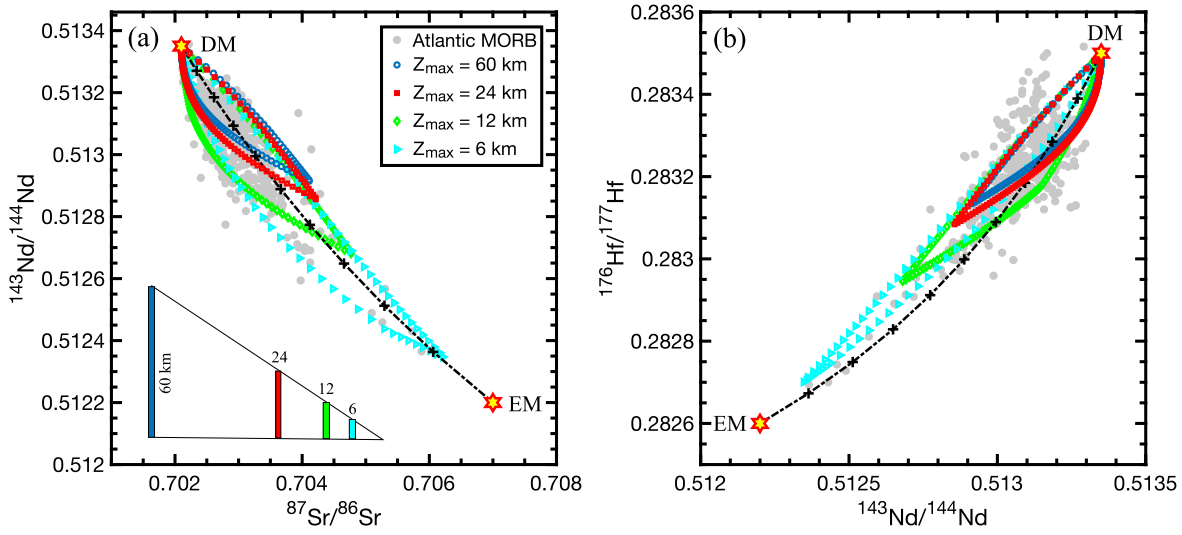

Fig. 6. Variations of Sr-Nd (a) and Nd-Hf (b) isotope ratios in pooled melts produced by melting a modally heterogeneous mantle. The mantle source consists of 8% orthopyroxenite (2.5% cpx + 17.5% olivine + 80% opx, EM) and 92% spinel lherzolite (17% cpx + 27% opx + 53% olivine + 3% spinel, DM). The size of EM in the mantle source is 2.4 km and the spacing between two adjacent EM parcels is 27.6 km. The gray circles are MORB data from the compilation of Stracke (2012) for the Mid-Atlantic Ridge. Other color-coded symbols represent pooled melts calculated from four upwelling columns (vertical bars in the inset to panel a) that are positioned at selected distances from the ridge axis. For simplicity, we use modal melting for the orthopyroxenite and nonmodal melting (Eq. (16a)) for spinel lherzolite. For reference, binary mixing lines derived from mixing of pooled melts produced by 15% fractional melting of the pure DM and EM are shown as dash-dotted lines with 10% increments marked by the plus symbols.

for a given enriched melt fraction. This is in stark contrast to the time-dependent model in which mixing between enriched melts and depleted melts derived from the two mantle sources at various depths in the melting column produces a mixing loop that is rotated either counter-clockwise or clockwise away from the simple mixing line in the isotope ratio correlation diagram (Figs. 4–6). This is a unique feature of mixing of melts derived from a spatially heterogeneous mantle (Rudge et al., 2013; Liu and Liang, 2020). In spite of the noted differences, the average composition of all the melts in a complete mixing loop is plotted on the binary mixing line. The average $^{87}Sr/^{86}Sr$ of all the melts in the mixing loop is calculated from the sum of concentrations of individual isotope in the pooled melt accumulated at each time step (j) using the expression:

$$\left(\frac{^{87}Sr}{^{86}Sr}\right)_{avg\_melt} = \frac{\sum_{j=1}^{N} C_{f,j}^{pool,87}}{\sum_{j=1}^{N} C_{f,j}^{pool,86}}, \tag{17a}$$

where N is the total number of samples in a mixing loop. The average isotope composition is shown as the green square in Fig. 4 and the green square and blue circle in Fig. 5. This is a consequence of global mass conservation, as the weight fraction of EM in a complete mixing loop is the same as that in the binary mixing calculation. Liu and Liang (2020) further demonstrated this point using a 2D ridge model in which spheres of chemically heterogeneous mantle are embedded in the ambient depleted mantle. Since isotope ratio is not a conserved quantity, the average of isotope ratios of melts in a complete mixing loop (triangles in Fig. 5) fall off the binary mixing line. The average of isotope ratios is calculated from isotope ratio of the pooled melt at each time step (R_j) using the expression:

$$R_{avg\_ratio} = \frac{1}{N}\sum_{j=1}^{N} R_j. \tag{17b}$$

Hence the average of isotope ratios in a suite of basalts is not representative of the average isotope ratio of the mantle source.

5.3. Application to Sr-Nd-Hf variations in MORB

Fig. 6 presents an application of the time-dependent melting model to variations of Sr, Nd, and Hf isotope ratios in MORB samples from the Mid-Atlantic Ridge (gray circles). The two-lithology mantle source consists of orthopyroxenite (2.5% cpx + 17.5% olivine + 80% opx, EM) and spinel lherzolite (17% cpx + 27% opx + 53% olivine + 3% spinel, DM). The size of EM is 2.4 km; the spacing between two adjacent EM parcels is 27.6 km; and the volume fraction of EM in the mantle source is 8%. To model melting beneath mid-ocean ridge, we subdivide the triangular melting region into vertical columns (inset to Fig. 6a) and use Eqs. (9), (14), and (15) to calculate Sr, Nd, and Hf concentrations and isotope ratios in the pooled melt at the top of each column. In this bundle of columns ridge model, the height of melting column decreases with the distance away from the ridge axis. Fig. 6 shows results of calculated pooled melt compositions from four columns with heights of 6, 12, 24, and 60 km and maximum extents of melting of 1.5%, 3%, 6%, and 15%, respectively. The aspect ratio of the mixing loop depends on the height of the melting column and the spacing between two adjacent EM parcels. When the height of a melting column is taller than the spacing of EM parcels, the number and volume fraction of EM in the melting column do not vary significantly. Consequently, compositions of the pooled melt from the tall melting columns do not differ significantly from each other. This explains the similarity between the 60 km and 24 km mixing loops in Fig. 6 (blue and red symbols). However, when the height of the melting column is significantly shorter than the spacing of EM parcels, there are no more than one EM parcel in the melting column at a time. The pooled melt is most enriched when there is one EM parcel in the melting column, but most depleted when there is no EM in the melting column. The largest variations come from the shortest melting column (6 km in Fig. 6) where the relative size or volume fraction of EM in the melting column is the largest (2.4/6 or 40%). The combination of smaller degree of melting and larger relative EM size gives rise to the more enriched signals in the pooled melts from the shorter melting columns. With decreasing column height, the most enriched point of a mixing loop converges toward the EM endmember. Since shorter melting columns produce less amount of melt than taller

columns, their contribution to eruptible melts beneath the ridge axis is small. (For example, it is 10 times more likely to sample melts from the 60 km column than melts from the 6 km column.) This provides a simple explanation to the sparse long tail defined by the more enriched MORB samples in the isotope ratio correlation diagrams (Figs. 6a and 6b). The majority of MORB samples are plotted just below the DM endmember forming an elongated cluster that is enclosed by the mixing loops produced by the taller melting columns. With additional mixing of melts derived from different melting columns along the slope of the melting triangle and/or in the axial magma chamber, which is not treated here, it is possible to account for most of the variations observed in the MORB samples shown in Fig. 6. However, these additional mixing will reduce the variabilities of Sr, Nd, and Hf isotope ratios, which can be offset by an increase in EM size or Sr, Nd, and Hf concentrations in the EM source. (A reader is referred to Liu and Liang (2017 and 2020) for a detailed discussion of the trade-offs among the size, concentration, and melt pooling area.) Hence the 2.4 km is likely a lower bound for the mean heterogeneity size. This is in good agreement with the inferred heterogeneity size based on 2D numerical studies of melting a spatially distributed and chemically heterogeneous mantle beneath mid-ocean ridge spreading centers (Liu and Liang, 2017, 2020).

6. Summary and further discussion

During decompression melting, spatial locations of different lithologies change continuously as a function of time in the melting column, which needs to be considered in a melting model. This study presents a set of conservation equations that can be used to keep track of spatial and temporal variations of mineral mode, melting rate, melting reaction, extent of melting, and bulk partition coefficient of a trace element in different lithologies in the melting column (Eqs. (2)-(6)). These equations follow the motion of residual solid in the upwelling mantle and can be readily generalized to higher dimensions. The usefulness of the new model is demonstrated through a simplified problem of melting a modally heterogeneous mantle in which the enriched and depleted lithologies have the same melting rate. This reduced problem has an exact solution (Eqs. (8)-(11)) that is similar to the well-known problem of melting a homogeneous mantle. The key difference between the two is the travel time (Eq. (9c)) which describes the location of a mantle parcel at a given time in the melting column. To model trace element fractionation, one starts with the mass conservation equation (Eq. (12)). The lithology implicitly appears in the melting model through the time-dependent boundary condition and the bulk partition coefficient. An exact solution for the time-dependent perfect fractional melting is presented (Eqs. (14) and (15)). This new solution is reduced to known expressions for perfect fractional melting of a homogeneous mantle (Shaw, 1970) and a chemically heterogeneous mantle (Liang and Liu, 2018) under limiting conditions. Essential features of the time-dependent perfect fractional melting model are explained and discussed through case studies of melting a two-lithology mantle that consists of the depleted lherzolitic mantle and an enriched pyroxenitic mantle. The main results can be summarized as follows:

1. To model melting a lithologically heterogeneous mantle, one follows the trajectory of residual solid in the melting column. In a frame of reference moving with residual solid, the time-dependent perfect fractional melting model is identical to the standard perfect fractional melting model (Shaw, 1970) that has been widely used in the geochemical literature.
2. With different lithologies constantly moving in the melting column, composition of pooled melt varies as a function of time. This is the key difference between decompression melting of a homogeneous mantle and a spatially heterogeneous mantle. Mixing of melts derived from the enriched and depleted mantle sources at different locations in the melting column gives rise to mixing loops that rotate away from simple mixing lines in the Sr-Nd-Hf isotope ratio correlation diagrams. The proportion of samples from the enriched and depleted branches in a complete mixing loop is the same as the proportion of EM and DM in the mantle source. These are unique features of melting a spatially heterogeneous mantle, and offer a simple explanation to the scattered correlations and sparse long tails in Sr-Nd-Hf isotope ratio correlation diagrams for basalt samples.
3. The role of lithological heterogeneity is to change the bulk partition coefficient of a trace element from its values in the lherzolitic mantle to new values in the lithologically distinct mantle. Consequently, the extent of depletion or residence time of the trace element in the melting column is changed compared to the case of melting a chemically heterogeneous mantle or a homogeneous mantle. Changing bulk partition coefficient with time and space results in greater variabilities in highly incompatible trace element concentrations and isotope ratios in the pooled melt. In the presence of opx-rich lithology, it is possible to produce extreme fractionations in incompatible trace element concentrations and isotope ratios.
4. Results from this study highlight the importance of spatially heterogeneous mantle source to the interpretation of chemical and isotope ratio variations observed in basalts. Binary mixing model cannot explain the extreme fractionation of highly incompatible trace elements in the pooled melt, and the mixing loop and its rotation in the isotope ratio correlation diagram. With increasing sample density, the time averaged pooled melt converges towards the melt composition determined by the simple binary mixing model.

Results from this study establish a framework for systematic studies of trace element fractionation and isotope ratio variation during decompression melting of a spatially distributed and lithologically heterogeneous mantle. As a first study of its kind, a simplified problem of melting a modally heterogeneous mantle is considered. The assumptions of equal melting rate and local chemical equilibrium will not affect the main conclusions presented in this study. Higher melting rate of the enriched lithology results in greater depletion of the incompatible trace element in the melting column, which will lead to an increase in variabilities of incompatible trace elements and Sr-Nd-Hf isotope ratios in the pooled melt. Chemical disequilibrium, on the other hand, hinders the depletion of incompatible trace element in residual solid, which acts to reduce the chemical variabilities in the pooled melt. There is no melt percolation in the perfect fractional melting model. In a more realistic case in which the porosity is not zero in the residual mantle, the enriched chemical signal of an incompatible trace element will be carried by the percolating melt, whereas the lithological heterogeneity will move with the residual mantle. Because the flow rate of the melt is higher than that of the solid, the chemical and lithological heterogeneities will be decoupled in the melting column. Supplementary Movie_4.mp4 previews one such case in which 65% of melt are extracted through channels ($\mathbb{R} = 0.65$ in Eq. (B.2)). These more general cases are subjects of future studies.

The present study also helps to identify parameters that are important to understanding trace element fractionation during decompression melting of a lithologically heterogeneous mantle. These include: melting rates, melting reactions, mineral-melt partition coefficients, and starting mantle compositions of the enriched and depleted lithologies. These melting parameters are relatively well known for the lherzolitic mantle, but considerably less constrained for other mantle lithologies or enriched compo-

nents. With proper choices of the latter, models similar to the ones shown in Figs. 4–6 can reproduce most of the observed $^{87}Sr/^{86}Sr$, $^{143}Nd/^{144}Nd$, and $^{176}Hf/^{177}Hf$ variations in global MORB and OIB.

CRediT authorship contribution statement

Yan Liang: Conceptualization, Funding acquisition, Investigation, Methodology, Visualization, Writing.

Declaration of competing interest

The author declares that he has no known competing financial interests or personal relationships that could have appeared to influence the work reported in this paper.

Acknowledgements

I thank Boda Liu and Soumen Mallick for useful discussion and helpful comments on earlier versions of the manuscript, Giulio Borghini and Sarah Lambart for useful discussion on the pyroxenite melting reaction. Thoughtful reviews by two anonymous reviewers helped to improve the manuscript. This work was supported by National Science Foundation grant OCE-1852088.

Appendix A. Evolution equation for k_m

Consider melting and melt migration in a 1D upwelling column in which a fraction of melt generated ($\mathbb{R}$) is extracted to nearby high-porosity channels. Mass conservation equations for the partial melt and bulk residual solid in the melting column are (McKenzie, 1984; Liang and Parmentier, 2010):

$$\frac{\partial \rho_f \phi_f}{\partial t} + \frac{\partial \rho_f \phi_f V_f}{\partial z} = \Gamma (1 - \mathbb{R}), \tag{A.1}$$

$$\frac{\partial \rho_s (1-\phi_f)}{\partial t} + \frac{\partial \rho_s (1-\phi_f) V_s}{\partial z} = -\Gamma. \tag{A.2}$$

We use mass conservation equation for a mineral in the residual solid to track mineral mode in the melting column (Liang et al., 2010):

$$\frac{\partial \rho_j \phi_j}{\partial t} + \frac{\partial \rho_j \phi_j V_s}{\partial z} = -p_j \Gamma. \tag{A.3}$$

The melting rate of mineral j is related the bulk solid melting rate (Γ) by the coefficient in the melting reaction p_j. To obtain an evolution equation for the bulk partition coefficient k_m, we multiply Eq. (A.3) by the mineral-melt partition coefficient, k_j:

$$k_j \frac{\partial \rho_j \phi_j}{\partial t} + k_j \frac{\partial \rho_j \phi_j V_s}{\partial z} = -p_j k_j \Gamma, \tag{A.4}$$

which can also be written as:

$$\frac{\partial \rho_j \phi_j k_j}{\partial t} + \frac{\partial \rho_j \phi_j V_s k_j}{\partial z} = -p_j k_j \Gamma + \rho_j \phi_j \left[\frac{\partial k_j}{\partial t} + V_s \frac{\partial k_j}{\partial z} \right]. \tag{A.5}$$

If k_j is a function of F, we have from chain rule:

$$\frac{\partial \rho_j \phi_j k_j}{\partial t} + \frac{\partial \rho_j \phi_j V_s k_j}{\partial z} = -p_j k_j \Gamma + \rho_j \phi_j \frac{\partial k_j}{\partial F} \left[\frac{\partial F}{\partial t} + V_s \frac{\partial F}{\partial z} \right]. \tag{A.6}$$

Summing Eq. (A.6) over all the minerals in residue, we have

$$\frac{\partial \sum_{j=1}^{N} \rho_j \phi_j k_j}{\partial t} + \frac{\partial \sum_{j=1}^{N} \rho_j \phi_j V_s k_j}{\partial z} = -\sum_{j=1}^{N} p_j k_j \Gamma + \left[\frac{\partial F}{\partial t} + V_s \frac{\partial F}{\partial z} \right] \sum_{j=1}^{N} \rho_j \phi_j \frac{\partial k_j}{\partial F}. \tag{A.7}$$

Recalling definitions of the bulk partition coefficient (k_m) and the partition coefficient according to melting reaction (k_m^p),

$$k_m = \sum_{j=1}^{N} w_j k_j, \tag{A.8}$$

$$k_m^p = \sum_{j=1}^{N} p_j k_j, \tag{A.9}$$

we have:

$$\frac{\partial \rho_s (1-\phi_f) k_m}{\partial t} + \frac{\partial \rho_s (1-\phi_f) V_s k_m}{\partial z} = -\Gamma k_m^p + \left[\frac{\partial F}{\partial t} + V_s \frac{\partial F}{\partial z} \right] \sum_{j=1}^{N} \rho_j \phi_j \frac{\partial k_j}{\partial F}. \tag{A.10}$$

With the help of Eq. (A.2), we obtain a general evolution equation for the bulk solid-melt partition coefficient for a trace element in the melting column:

$$\frac{\partial k_m}{\partial t} + V_s \frac{\partial k_m}{\partial z} = \frac{\Gamma}{\rho_s (1-\phi_f)} \left[k_m - k_m^p + (1-F) \sum_{j=1}^{N} w_j \frac{\partial k_j}{\partial F} \right]. \tag{A.11}$$

To obtain the working Eq. (4), we combine Eq. (3) and Eq. (A.11):

$$\frac{\partial (1-F) k_m}{\partial t} + V_s \frac{\partial (1-F) k_m}{\partial z} = -\frac{(1-F)\Gamma}{\rho_s (1-\phi_f)} \left[k_m^p - (1-F) \sum_{j=1}^{N} w_j \frac{\partial k_j}{\partial F} \right]. \tag{A.12}$$

The summation term on the right-hand side of Eqs. (A.11) and (A.12) can also be replaced by the bulk partition coefficient using the identity:

$$\frac{\partial k_m}{\partial F} = \sum_{j=1}^{N} w_j \frac{\partial k_j}{\partial F}. \tag{A.13}$$

When the mineral-melt partition coefficient (k_j) is constant and uniform in the melting column, Eqs. (A.11) and (A.12) are simplified to Eqs. (2) and (4) used in the present study.

Appendix B. Mass conservation equation for a trace element

We start with the total mass conservation equation for a trace element in the partial melt and bulk residual solid in the melting column (Liang and Peng, 2010):

$$\frac{\partial \left[\rho_f \phi_f C_f + \rho_s (1-\phi_f) C_s \right]}{\partial t} + \frac{\partial \left[\rho_f \phi_f V_f C_f + \rho_s (1-\phi_f) V_s C_s \right]}{\partial z} = -C_f \mathbb{R} \Gamma. \tag{B.1}$$

When the solid and melt are local chemical equilibrium, $C_s = k_m C_f$, Eq. (B.1) becomes:

$$\frac{\partial \left[\rho_f \phi_f + \rho_s (1-\phi_f) k_m \right] C_f}{\partial t} + \frac{\partial \left[\rho_f \phi_f V_f + \rho_s (1-\phi_f) V_s k_m \right] C_f}{\partial z} = -C_f \mathbb{R} \Gamma. \tag{B.2}$$

Expanding the products in the time and spatial derivatives in Eq. (B.2), we have

$$\left[\rho_f\phi_f+\rho_s\left(1-\phi_f\right)k_m\right]\frac{\partial C_f}{\partial t}+\left[\rho_f\phi_f V_f+\rho_s\left(1-\phi_f\right)V_s k_m\right]\frac{\partial C_f}{\partial z}+C_f\left\{\frac{\partial \rho_f\phi_f}{\partial t}+\frac{\partial \rho_f\phi_f V_f}{\partial z}\right\}+C_f\left\{\frac{\partial \rho_s\left(1-\phi_f\right)k_m}{\partial t}+\frac{\partial \rho_s\left(1-\phi_f\right)V_s k_m}{\partial z}\right\}=-C_f\mathbb{R}\Gamma. \tag{B.3}$$

Replacing terms in curly brackets through Eqs. (A.1) and (A.11), we obtain a general mass conservation equation for a trace element in the upwelling column in which partition coefficients vary spatially and temporally during melting:

$$\left[\rho_f\phi_f+\rho_s\left(1-\phi_f\right)k_m\right]\frac{\partial C_f}{\partial t}+\left[\rho_f\phi_f V_f+\rho_s\left(1-\phi_f\right)V_s k_m\right]\frac{\partial C_f}{\partial z}=\Gamma\left[k_m^p-1-(1-F)\sum_{j=1}^{N}w_j\frac{\partial k_j}{\partial F}\right]C_f. \tag{B.4}$$

Substituting Eq. (A.13) into Eq. (B.4), we recover the mass conservation Eq. (A8) of Liang and Peng (2010):

$$\left[\rho_f\phi_f+\rho_s\left(1-\phi_f\right)k_m\right]\frac{\partial C_f}{\partial t}+\left[\rho_f\phi_f V_f+\rho_s\left(1-\phi_f\right)V_s k_m\right]\frac{\partial C_f}{\partial z}=\Gamma\left[k_m^p-1-(1-F)\frac{\partial k_m}{\partial F}\right]C_f. \tag{B.5}$$

In general, the mineral-melt partition coefficient k_j is a function of temperature, pressure, and major element compositions of the mineral and coexisting melt. It is possible to parameterize k_j or k_m as a function of F in a melting model. Eqs. (B.4) and (B.5) are master equations for modeling trace element fractionation during melting and melt transport in a partially molten solid in which residual minerals and interstitial melt are in local chemical equilibrium.

Appendix C. Supplementary material

Supplementary material related to this article can be found online at https://doi.org/10.1016/j.epsl.2020.116594.

References

Baker, M.B., Stolper, E.M., 1994. Determining the composition of high-pressure mantle melts using diamond aggregates. Geochim. Cosmochim. Acta 58, 2811–2827.

Bo, T., Katz, R.F., Shorttle, O., Rudge, J.F., 2018. The melting column as a filter of mantle trace-element heterogeneity. Geochem. Geophys. Geosyst. 19, 4694–4721.

Borghini, G., Fumagalli, P., Rampone, E., 2017. Partial melting of secondary pyroxenite at 1 and 1.5 GPa and its role in upwelling heterogeneous mantle. Contrib. Mineral. Petrol. 172, 70.

Dasgupta, R., Jackson, M.G., Lee, C-T.A., 2010. Major element chemistry of ocean island basalts – conditions of mantle melting and heterogeneity of mantle source. Earth Planet. Sci. Lett. 289, 377–392.

DePaolo, D.J., 1996. High-frequency isotopic variations in the Mauna Kea tholeiitic basalt sequence: melt zone dispersivity and chromatography. J. Geophys. Res. 101, 11855–11864.

Elkins, L.J., Bourdon, B., Lambart, S., 2019. Testing pyroxenite verse peridotite sources for marine basalts using U-series isotopes. Lithos 332–333, 226–244.

Hirschmann, M.M., Stolper, E.M., 1996. A possible role for garnet pyroxenite in the origin of the "garnet signature" in MORB. Contrib. Mineral. Petrol. 124, 185–208.

Hirschmann, M.M., Kogiso, T., Baker, M.B., Stolper, E.M., 2003. Alkalic magmas generated by partial melting of garnet pyroxenite. Geology 31, 481–484.

Hofmann, A.W., 2014. Sampling mantle heterogeneity through oceanic basalts: isotopes and trace elements. In: Carlson, R.W. (Ed.), Treatise on Geochemistry: the Mantle and Core, 2nd edition. Elsevier, New York, pp. 67–101.

Ito, G., Mahoney, J.J., 2005. Flow and melting of a heterogeneous mantle: 1. Method and importance to the geochemistry of ocean island and mid-ocean ridge basalts. Earth Planet. Sci. Lett. 230, 29–46.

Kogiso, T., Hirose, K., Takahashi, E., 1998. Melting experiments on homogeneous mixtures of peridotite and basalt: application to the genesis of ocean island basalts. Earth Planet. Sci. Lett. 162, 45–61.

Lambart, S., Laporte, D., Schiano, P., 2009. An experimental study of pyroxenite partial melts at 1 and 1.5 GPa: implications for the major-element composition of Mid-Ocean Ridge Basalts. Earth Planet. Sci. Lett. 288, 335–347.

Lambart, S., Baker, M.B., Stolper, E.M., 2016. The role of pyroxenite in basalt genesis: melt-PX, a melting parameterization for mantle pyroxenites between 0.9 and 5 GPa. J. Geophys. Res. 121, 5708–5735.

Langmuir, C.H., Vocke Jr., R.D., Hanson, G.N., Hart, S.R., 1978. A general mixing equation with applications to Icelandic basalts. Earth Planet. Sci. Lett. 37, 380–392.

Liang, Y., 2008. Simple models for dynamic melting in an upwelling heterogeneous mantle column: analytical solutions. Geochim. Cosmochim. Acta 72, 3804–3821.

Liang, Y., Liu, B., 2018. Stretching chemical heterogeneity by melt migration in an upwelling mantle: an analysis based on time-dependent batch melting and fractional melting models. Earth Planet. Sci. Lett. 498, 275–287.

Liang, Y., Parmentier, E.M., 2010. A two-porosity double lithology model for partial melting, melt transport and melt–rock reaction in the mantle: mass conservation equations and trace element transport. J. Petrol. 51, 125–152.

Liang, Y., Peng, Q., 2010. Non-modal melting in an upwelling mantle column: steady-state models with applications to REE depletion in abyssal peridotites and the dynamics of melt migration in the mantle. Geochim. Cosmochim. Acta 74, 321–339.

Liang, Y., Schiemenz, A., Hesse, M., Parmentier, E.M., Hesthaven, J.S., 2010. High-porosity channels for melt migration in the mantle: top is the dunite and bottom is the harzburgite and lherzolite. Geophys. Res. Lett. 37, L15306.

Liu, B., Liang, Y., 2017. The prevalence of kilometer-scale heterogeneity in the source region of MORB upper mantle. Sci. Adv. 3, e1701872.

Liu, B., Liang, Y., 2020. Importance of the size and distribution of chemical heterogeneities in the mantle source to the variations of isotope ratios and trace element abundances in mid-ocean ridge basalts. Geochim. Cosmochim. Acta 268, 383–404.

Lo Cascio, M., 2008. Kinetics of partial melting and melt-rock reaction in the Earth's mantle. Ph.D. Thesis. Brown University.

McDonough, W.F., Sun, S.S., 1995. The composition of the Earth. Chem. Geol. 120, 223–253.

McKenzie, D., 1984. The generation and compaction of partially molten rock. J. Petrol. 25, 713–765.

Morgan, Z., Liang, Y., 2005. An experimental study of the kinetics of lherzolite reactive dissolution with applications to melt channel formation. Contrib. Mineral. Petrol. 150, 369–385.

Phipps Morgan, J., 1999. Isotope topology of individual hotspot basalt arrays: mixing curves or melt extraction trajectories? Geochem. Geophys. Geosyst. 1, 1003.

Prytulak, J., Elliott, T., 2007. TIO2 enrichment in ocean island basalts. Earth Planet. Sci. Lett. 263, 388–403.

Richter, F.M., Daly, S.F., 1989. Dynamical and chemical effects of melting a heterogeneous source. J. Geophys. Res. 94, 12499–12510.

Rudge, J.F., Maclennan, J., Stracke, A., 2013. The geochemical consequences of mixing melts from a heterogeneous mantle. Geochim. Cosmochim. Acta 114, 112–143.

Shaw, D.M., 1970. Trace element fractionation during anatexis. Geochim. Cosmochim. Acta 34, 237–243.

Sobolev, A.V., Hofmann, A.W., Nikogosian, I.K., 2000. Recycled oceanic crust observed in 'ghost plagioclase' within the source of Mauna Loa lavas. Nature 404, 986–989.

Sobolev, A.V., Hofmann, A.W., et al., 2007. The amount of recycled crust in sources of mantle derived melts. Science 316, 412–417.

Stracke, A., 2012. Earth's heterogeneous mantle: a product of convection-driven interaction between crust and mantle. Chem. Geol. 330–331, 274–299.

Stracke, A., Bourdon, B., 2009. The importance of melt extraction for tracing mantle heterogeneity. Geochim. Cosmochim. Acta 73, 218–238.

Sun, C., Liang, Y., 2013. Distribution of REE and HFSE between low-Ca pyroxene and lunar picritic melts around multiple saturation points. Geochim. Cosmochim. Acta 119, 340–358.

Takahashi, E., Nakajima, K., Wright, T.L., 1998. Origin of the Columbia river basalts: melting model of a heterogeneous plume head. Earth Planet. Sci. Lett. 162, 63–80.

Vollmer, R., 1976. Rb-Sr and U-Th-Pb systematics of alkaline rocks: the alkaline rocks from Italy. Geochim. Cosmochim. Acta 40, 283–295.

Walter, M., 2014. Melt extraction and compositional variability in mantle lithosphere. In: Carlson, R.W. (Ed.), Treatise on Geochemistry: the Mantle and Core, 2nd edition. Elsevier, New York, pp. 393–419.

Wang, C., Lo Cascio, M., Liang, Y., Xu, W., 2020. An experimental study of peridotite dissolution in eclogite-derived melts: implications for styles of melt-rock interaction in lithospheric mantle beneath the North China Craton. Geochim. Cosmochim. Acta 278, 157–176.

Wanless, V.D., Behn, M.D., Shaw, A.M., Plank, T., 2014. Variations in melting dynamics and mantle compositions along the Eastern Volcanic Zone of the Gakkel Ridge: insights from olivine-hosted melt inclusions. Contrib. Mineral. Petrol. 167, 1005.
White, W.M., 2010. Oceanic island basalts and mantle plumes: the geochemical perspective. Annu. Rev. Earth Planet. Sci. 38, 133–160.
Workman, R.K., Hart, S.R., 2005. Major and trace element composition of the depleted MORB mantle (DMM). Earth Planet. Sci. Lett. 231, 53–72.
Yao, L., Sun, C., Liang, Y., 2012. A parameterized model for REE distribution between low-Ca pyroxene and basaltic melts with applications to REE partitioning in low-Ca pyroxene along a mantle adiabat and during pyroxenite-derived melt and peridotite interaction. Contrib. Mineral. Petrol. 164, 261–280.
Yaxley, G.M., Green, D.H., 1998. Reactions between eclogite and peridotite: mantle refertilisation by subduction of oceanic crust. Schweiz. Mineral. Petrogr. Mitt. 78, 243–255.
Zindler, A., Hart, S., 1986. Chemical geodynamics. Annu. Rev. Earth Planet. Sci. 14, 493–571.